Advances in Aerodynamics

RESEARCH Open Access

Experimental study of bluntness effects on hypersonic boundary-layer transition over a slender cone using surface mounted pressure sensors

Ranran Huang[1], Jiangyi Cheng[1], Jianqiang Chen[2,3], Xianxu Yuan[2,3] and Jie Wu[1*]

*Correspondence:
jiewu@hust.edu.cn

[1] School of Aerospace Engineering, Huazhong University of Science and Technology, Wuhan 430074, People's Republic of China
[2] State Key Laboratory of Aerodynamics, China Aerodynamics Research and Development Center, Mianyang 621000, People's Republic of China
[3] Computational Aerodynamics Institute, China Aerodynamics Research and Development Center, Mianyang, 621000, People's Republic of China

Abstract

In this work, we studied the bluntness effect on the hypersonic boundary-layer transition over a slender cone at Mach 6 with interchangeable tips in a noisy Ludwieg tube tunnel before the so-called "transition reversal" phenomenon occurs. The evolution of instability waves is characterized using surface flush-mounted pressure sensors deployed along the streamwise direction within unit Reynolds number from $4E+6/m \le Re_{unit} \le 10E+6/m$, and the bluntness of the cone nose ranges from 0.1 mm to 5 mm. Power spectral density (PSD) of pressure fluctuation indicates that small nose bluntness ($Re_R \le 2000$) has little influence on the evolution of instability waves along the hypersonic boundary-layer, whereas with a moderate nose size ($2000 \le Re_R \le 5000$), the hypersonic boundary layer transition is delayed monotonically as the nose radius increases before the boundary-layer turns into fully laminar without instability waves. The delaying effect can be attributed to the increased entropy-layer swallowing distance with a large tip radius. Instability wave characterization reveals that the second mode instability wave plays a dominant role before the transition reversal happens. The quadratic phase locking of second mode instabilities can be identified by bispectral analysis, and it attenuates as the nose tip radius increases.

Keywords: Hypersonic boundary-layer, Laminar/turbulent boundary-layer transition, Bluntness effect, Second mode

1 Introduction

To date, laminar/turbulent boundary-layer transition is still one of the most important issues in hypersonic aerodynamic and aerothermal design, as boundary-layer transition has a significant impact on the deployment of thermal protection systems and also trajectory design of hypersonic vehicles [1, 2]. Despite a quite large effort has been devoted to this topic in the past 70 years, only partial knowledge of hypersonic boundary-layer transition has been obtained so far due to the complexity of hypersonic instability waves [3–12], such as nose-tip bluntness of slender cone models. Previous research mainly focuses on sharp cone models, and its transition mechanism at different stages is well

understood by far [5, 13]. In practice, however, a blunt nose is preferred for the sake of stagnation heat flux reduction. Due to the existence of bow shock induced by the blunt nose-tip, the entropy-layer swallowing distance has been noticed to be an important parameter for the boundary-layer transition. Previous investigations show that the boundary-layer transition can be delayed by increasing the nose-tip bluntness, and as the nose-tip reaches a certain size, the hypersonic boundary-layer turns turbulent abruptly, which is the so-called transition reversal phenomenon [5, 10]. Stetson et al. [14–16] conducted experimental investigations of a slender cone with different nose radiuses in hypersonic flows, and found that the instability waves developed in the entropy-layer might be the dominant instability waves and play an important role, even before transition reversal. Moreover, he noticed that in the transition reversal regime, the transition is relatively sensitive to the surface roughness in the nose-tip region. Almost at the same time, Softley [17] also performed the instability experiment in Mach 10 to 12 flows on blunt cones with 5 degrees half-angle and the transition reversal was observed between small and large bluntness, but no persuasive elaboration regarding this issue was given. More recently, the issue of nose-tip bluntness has re-attracted attention of the hypersonic transition research community, as blunt nose tip design is generally preferred in the practical design of hypersonic vehicles. Lei and Zhong [18] investigated the effect of nose bluntness using the Linear Stability Theory (LST) method, and they found that the hypersonic laminar boundary-layer is generally stabilized due to the downstream shifting of the linear stable region of second-mode instabilities, and no reversal on the growth of the second-mode instability was observed. They speculated that the transition reversal is caused by some uncontrolled noise with the amplitude larger enough that the growth of disturbance bypasses the linear region and forces the transition to occur earlier. Jewell and Kimmel [19] repeated Stetson's experiment using PSE code without satisfactory output as only the streamwise instability waves can be captured. Grossir et al. [20] further studied the influence of nose-tip bluntness on conical boundary-layer instabilities at Mach 10 using surface mounted pressure sensor and Schlieren. They found that with small to moderate nose-tip bluntness the hypersonic boundary-layer transition is delayed where the second mode instability is dominant. At large nose-tips, however, the second mode instabilities disappear and instabilities with different shapes were identified. Paredes et al. [21, 22] recently applied the non-modal disturbance in explaining transition onset in the entropy-layer, and large N factors for non-modal disturbance can be obtained whereas the N factors for modal instabilities are decreasing. Eventually they concluded that the non-modal disturbance analysis might be the key to explaining the transition reversal with a large nose-tip and a possible competitive mechanism may exist between the modal and non-modal disturbances. More recently, Kennedy et al. [23] performed experiments to investigate the effect of nose-tip bluntness on the instability mechanism leading to boundary layer transition, and non-modal features were captured by the calibrated Schlieren when a large radius of nose was employed with a high freestream Reynolds number. They conjectured that a possible connection might exist between the two instability mechanisms.

In review of the previous work, it appears that the mechanism that leads to boundary-layer instability and transition on blunt geometries is not well understood yet, despite the general consensus agreed on the rearward shifting of linear stable region

when the entropy-layer is introduced by blunt bodies [15, 20]. The completive relationship between instabilities orientated from the entropy-layer and the instabilities prescribed by the linear stability theory seems to be the focus of explaining the influence of blunt nose-tip on the hypersonic boundary-layer transition problem. Motivated by the preference for blunt nose-tip in practical vehicle design, a better understanding of the influence of bluntness on the hypersonic boundary-layer transition is thus of significant importance. In this work, we study the bluntness effect on hypersonic boundary-layer transition over a slender cone with interchangeable tips in a Mach 6 Ludwieg tube tunnel using surface flush-mounted pressure sensors under noisy status. To ensure the reliability of the experimental results, we first measured the disturbance level of the wind tunnel before the study. The content of this work is organized as follows: the experimental set-up and diagnostics are introduced first, together with the data-postprocessing; then the instability experiment of a slender cone model with different nose tips is performed, and the evolution of the instability waves with different nose-tip radii is characterized before the final conclusions are made.

2 Experimental set-up and diagnostics

2.1 Mach 6 Ludwieg tube tunnel

The experiment is conducted in the newly built Φ250 Mach 6 Ludwieg tube tunnel at Huazhong University of Science and Technology (HUST) [24], as shown in Fig. 1. The principle of conventional hypersonic Ludwieg tube has been comprehensively elaborated in [24–26], thus a brief introduction will be given herewith. The high-pressure air in the storage tube is separated from the downstream sections by a fast-acting valve. As the valve located at the throat opens, the pressurized air expands into the Laval nozzle, thereby generating a hypersonic flow depending on the area-ratio between the test section and the throat. Since the valve opens relatively fast, this process can be considered impulsive and the expansion waves can be treated as centered expansion waves. The expansion waves will travel upstream, and the flow after expansion defines the stagnation flow conditions for the tunnel's operation. Afterward, the expansion waves reach the end of the storage tube, and they will be reflected back towards the Laval nozzle's contraction. The fast-acting valve is closed when the reflected waves reach the nozzle's contraction. Meanwhile, the high-pressure air will rush into the Laval nozzle and expand to a hypersonic flow. The efficient running time of this Ludwieg tube is above 100 ms. To

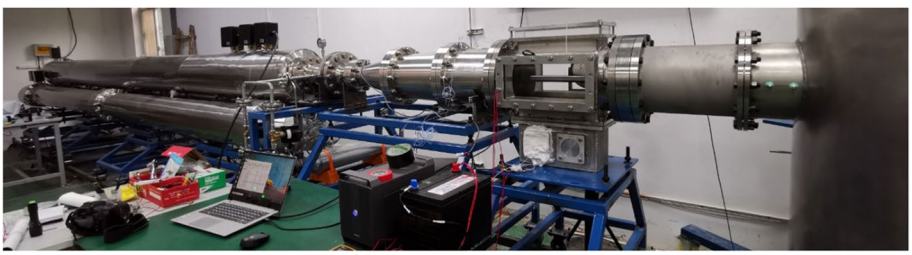

Fig. 1 Mach 6 Ludwieg tube tunnel in Huazhong University of Science and Technology

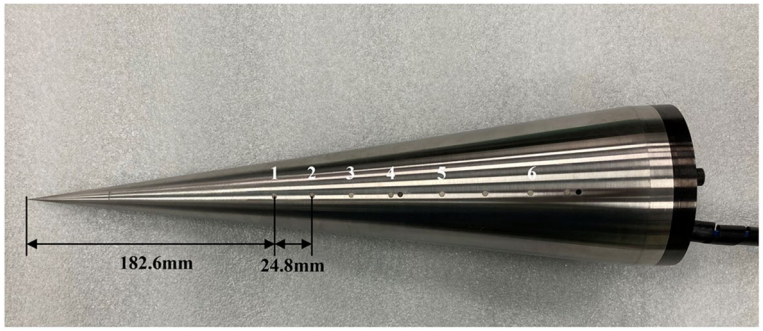

Fig. 2 7-degree half-angle cone model instrumented with PCB sensors

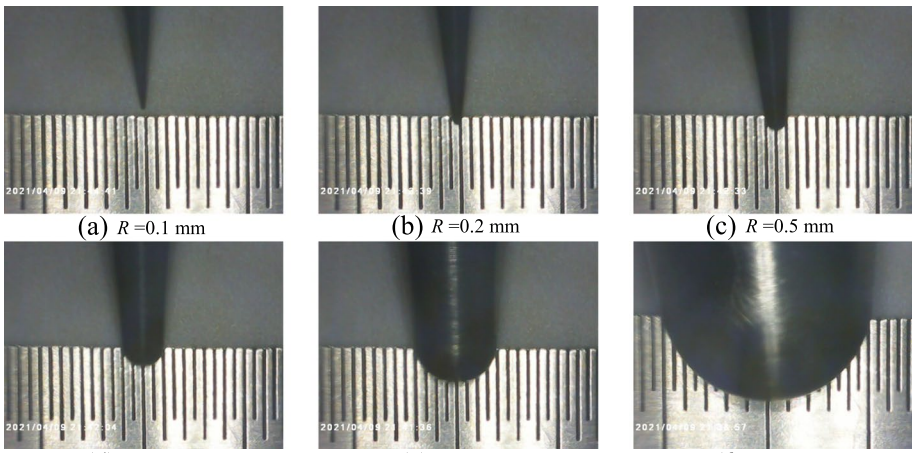

Fig. 3 Cone tip with different bluntness ranging from $R = 0.1$ mm to 5 mm

avoid flow condensation of the hypersonic freestream, the tunnel is generally heated up to 430 K, and to have natural transition phenomena, the stagnation pressure of the tunnel is adjustable from 3E+5 to 30E+5 Pa, resulting in a maximum unit Reynolds number of up to 30E+6/m.

2.2 Slender cone model

A 7-degree half-angle slender cone model is employed in this experiment, as shown in Fig. 2. The slender cone model has an overall length of 0.4 m, and it is comprised of three discs including an interchangeable cone tip. Limited by the length of the interchangeable cone tip, the radius of the nose-tip ranges from $R = 0.1$ mm to $R = 5.0$ mm, as shown in Fig. 3. The whole cone model is fabricated with stainless steel to promise a smooth connection between different disks, and the general surface roughness of the cone model is approximately 1.6 μm.

2.3 PCB sensors and data acquisition system

The PCB 132B38 piezoelectric pressure sensors are flush mounted on the cone model to measure the surface pressure fluctuation. This type of sensor has a diameter of 3.18 mm and an active quadratic area of $0.768 \times 0.768\,\text{mm}^2$. It is necessary to mention that the

132B38 sensors have been quantitatively calibrated before delivery and each is qualified with a sensitivity coefficient of about 19.7 mV/kPa (±30%), and the bandwidth of dynamic response ranges from 10 to 1000 kHz. For less uncertainty, the PCB data is generally limited to 1 MHz for data analysis. The power for the PCB sensor was supplied by two PCB instruments (M482A22 and M483A). In the present study, six PCB sensors are employed and installed axially along the cone as shown in Fig. 2. The time trace signals of PCB sensors are acquired with a Spectrum M2i.4652 transient recorder. The analog signal is stored in a 16-bit format. The sampling rate of the transient recorder is chosen to be 3 MHz, which is sufficient to resolve the instability waves expected in the measurement campaign.

3 Data analysis and reduction

3.1 Spectral analysis

The Fourier transform of time trace $S(t)$ and power spectrum are defined as:

$$S(f) = \lim_{T\to\infty} \frac{1}{T} \int_{-1/2T}^{1/2T} s(t) e^{-i2\pi ft} dt, \tag{1}$$

$$P(f) = E\big(S(f)S^*(f)\big), \tag{2}$$

where E denotes an expected value, S is the discrete Fourier transform, and the superscript * denotes the complex conjugation. The power spectral density is estimated using the Pwelch method with Hamming window (50% overlap, 1024 points per window), resulting in a frequency resolution of 2.9 kHz.

3.2 Cross-correlation

The cross-correlation is employed in characterizing the instability waves along the sharp cone mode for the PCB sensors based on the time delay. As a mathematical technique, cross-correlation calculates the similarity of two independent time transients as a function of a time-lag. The cross-correlation of the discrete functions is defined as:

$$Cross\ correlation[-] = \frac{\frac{1}{N}\sum_{n=1}^{N} V_{1,n} V_{2,n-i}}{\sigma_n \sigma_{n-i}}. \tag{3}$$

N is the number of discrete points, $V_{1,n}$ and $V_{2,n\text{-}i}$ are the amplitudes of the discrete points of each time trace signal, i is the time-lag point hereby and σ is the standard deviation of the time trace signals. As the time-lag of between the PCB sensors is calculated, the propagation velocity of the instability wave can be obtained.

3.3 Bicoherence analysis

Due to the co-existence of various instability waves in the hypersonic laminar boundary-layer, bispectrum is used to analyze the nonlinear phase-coupled interactions of instability waves. The bispectrum is a statistical method for evaluating the degree of phase coherence among a wave triad due to wave coupling [27].

$$B(f_1, f_2) = E\{S(f_1)S(f_2)S^*(f_1 + f_2)\}. \tag{4}$$

If the triad of waves f_1, f_2 and (f_1+f_2) are nonlinearly coupled, the bispectrum is a nonzero value. Compared with power spectrum, the bispectrum retains the information on the wave phase, allowing the identification of phase-coupled waves [28]. Since the value of bispectrum depends on the amplitude of wave, the bispectrum is generally thus normalized as follows,

$$b^2(f_1,f_2) = \frac{\left|B(f_1,f_2)\right|^2}{E\left[\left|S(f_1)S(f_2)\right|^2\right]E\left[\left|S(f_1+f_2)\right|^2\right]}. \tag{5}$$

By such normalization, the right-hand side of Eq. (4) is called bicoherence, indicating the degree of phase coupling with frequencies of f_1, f_2 and (f_1+f_2), however, with the value between 0 and 1. As the bicoherence is symmetry, the efficient area to calculate the bicoherence is restricted in the triangle region defined as Eq. (5), where f_N is the Nyquist frequency.

$$0 \le f_1 \le f_2, \quad f_1+f_2 \le \left(\frac{f_N}{2}\right). \tag{6}$$

In this work, the bicoherence is calculated from time-series data using a Hamming window with 50% overlap, and the points of each window are 1024. Considering that the sampling frequency of the data acquisition system is 3 MHz, the frequency resolution of the bicoherence comes to 2.9 kHz.

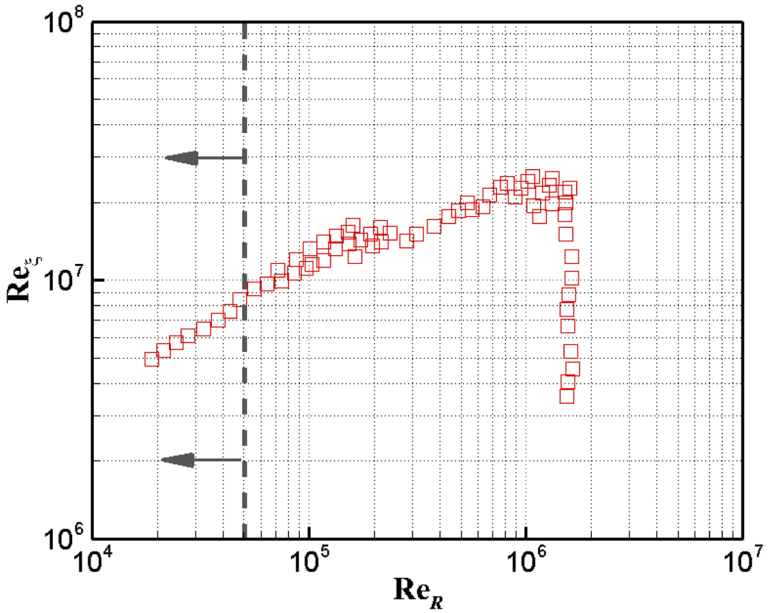

Fig. 4 Transition Reynolds number based on freestream as a function of the nose Reynolds number at Mach 6 by Stetson and Rushton [16]

4 Experimental results and analysis

The instability experiment is conducted in such a way that the unit Reynolds number of the freestream is adjusted by tuning the stagnation pressure of the wind tunnel from 4E+5 to 10E+5 Pa while the stagnation temperature is kept at 454 K, and this results in a maximum unit Reynolds number of 1E+7/m. Based on the maximum unit Reynolds number of the freestream, the maximum nose Reynolds number is 5E+4, which is marked out in the Fig. 4 transition reversal plot by Stetson and Rushton [16]. It is expected that within such a nose Reynolds number, the boundary-layer transition will be delayed monophonically.

The entropy-layer swallowing distance for the 7-degree half cone model at different freestream conditions is estimated using the method proposed by Rotta [29], as plotted in Fig. 5, which was validated previously by Stetson and Rushton [16]. It is obvious that the entropy-layer swallowing distance increases when the freestream Reynolds number and the nose radius increase. For a nose tip radius larger than 2 mm, the entropy-layer swallowing distance almost reaches the end of the cone model, whereas it is even larger than the cone length as the tip radius is 5 mm.

4.1 Disturbance level of hypersonic Ludwieg tube

Before the performance of instability experiment of the slender cone model, the freestream disturbance level of the Ludwieg tube tunnel is characterized by a Pitot probe instrumented with a PCB 132B38 pressure sensor. The pressure sensor is flush-mounted on the Pitot probe to avoid the Helmholtz resonance effect, and the Pitot probe is allocated at the centerline along the test section in accordance with

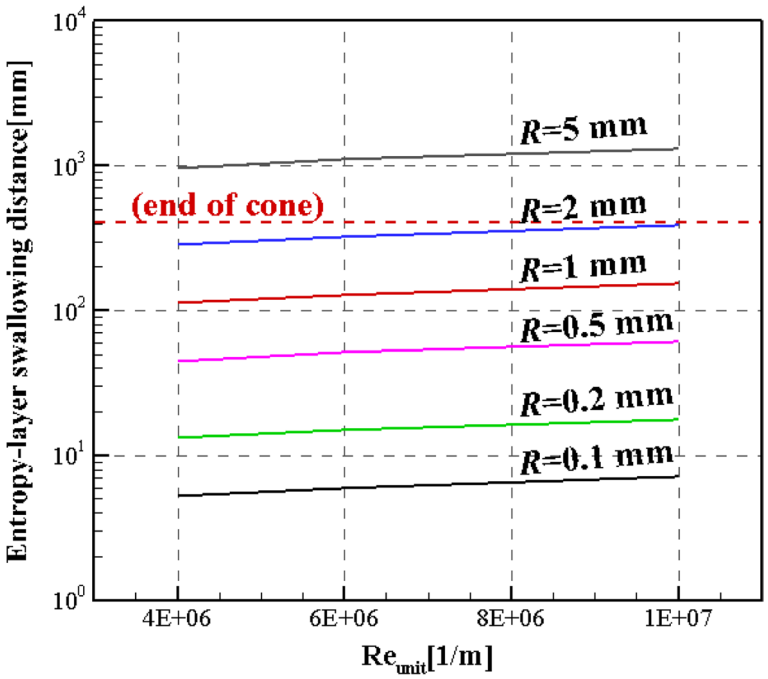

Fig. 5 Entropy-layer swallowing distance x_{sw} along 7-degree half angle slender cone model

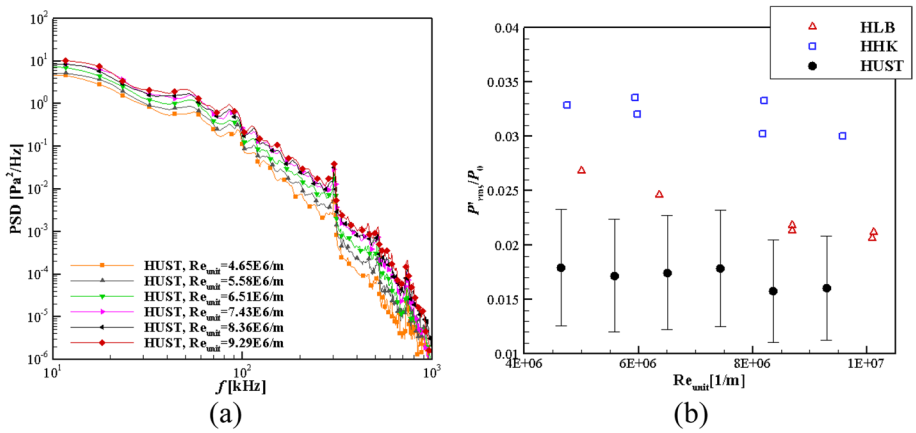

Fig. 6 Disturbance level characterization of the freestream. **a** PSD of Pitot pressure in the test section; **b** RMS of the normalized Pitot pressure fluctuation

Table 1 Entropy-layer swallowing distance along 7-degree half-angle cone model, $Re_{\text{unit}} = 4\text{E}+6/\text{m}$

Re_{unit} (1/m)	R (mm)	Ma	x_{sw} (mm)
4E+6	0.1	6	5.23
4E+6	0.2	6	13.18
4E+6	0.5	6	44.73
4E+6	1.0	6	112.71
4E+6	2.0	6	284.0
4E+6	5.0	6	963.62

the freestream measurement in the HHK wind tunnel of the United States Air Force Academy [30, 31]. The tunnel was operated over a large unit Reynolds number from 4.65E+6/m to 9.29E+6/m. Figure 6 shows the power spectral density (PSD) and the normalized root mean square (RMS) of Pitot pressure fluctuation in the HUST Ludwieg tube. At similar freestream Reynolds numbers, the disturbance level of the HUST Ludwieg tube is lower than that of the HHK and HLB Ludwieg tubes in general, which means the HUST Ludwieg tube is suitable for the hypersonic boundary-layer instability study.

4.2 Entropy-layer effect at a low Reynolds number $Re_{\text{unit}} = 4\text{E}+6/\text{m}$

For the convenience of analyzing the influence of entropy-layer swallowing distance upon the instabilities, the predicted entropy-layer swallowing distance along the cone model is listed in Table 1. At $Re_{\text{unit}} = 4\text{E}+6/\text{m}$ the entropy-layer swallowing distance changes from 5.23 mm to 963.32 mm when the radius of nose-tip increases from $R = 0.1$ mm to $R = 5$ mm. It is worth noting that the entropy-layer swallowing distance does not change much when the tip radius is smaller than 0.5 mm.

Figure 7 illustrates the PSD of pressure fluctuation along the cone surface with different nose-tips ranging from $R = 0.1$ mm to 5 mm at the same freestream Reynolds number, i.e., $Re_{\text{unit}} = 4\text{E}+6/\text{m}$. When the tip radius is 0.1 mm, the entropy-layer swallowing distance is relatively upstream of the first PCB sensor, and instability waves

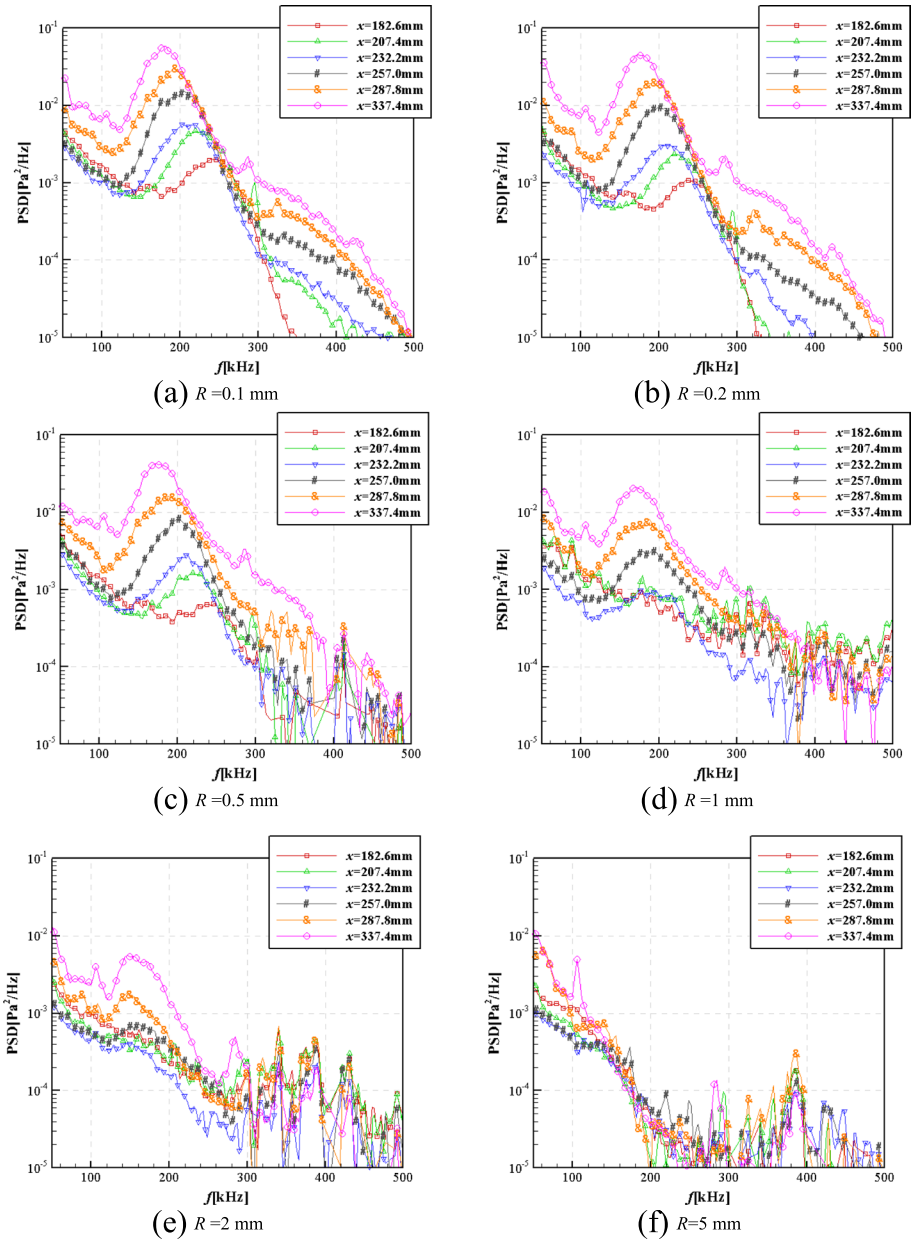

Fig. 7 PSD of wall pressure fluctuations at different cone bluntness. The wall temperature of the cone model is 300 K, the stagnation pressure of the wind tunnel is 4E+5 Pa, the stagnation temperature of the wind tunnel is 454 K, and the corresponding Reynolds number is 4E+6/m

ranging from 120 kHz to 300 kHz are observed all along the cone model, denoting a fully laminar boundary layer. The peak frequency of the instability waves shifts to a lower value as the flow propagates downstream with a thicker boundary-layer thickness. This property appears to be in line with that of the second mode instability waves referring to our previous measurement upon the same cone model at similar freestream conditions [25]. As the tip radius comes to $R = 0.2$ mm, the spectra of all 6 sensors are analogous to those of the case of $R = 0.1$ mm. However, a careful inspection of pressure spectra for PCB sensors located at $x = 182.6$ mm to 232.2 mm shows

that their amplitudes are slightly lower than those of the smaller cone tip case. At $R = 0.5$ mm the spectra amplitudes are similar except that the instability waves measured by the first PCB sensor appear to be more suppressed, as shown in Fig. 5(c). When the cone tip radius is 1 mm, it is interesting to see that the instability waves measured by the first three PCB sensors are strongly suppressed, and the broadband spectra amplitudes are generally smaller. Considering the predicted entropy-layer swallowing location x_{sw} for $R = 1$ mm is about 112.7 mm, the suppression of instabilities can be attributed to the rearward displacement of the linear stability region. From this aspect of view, the visible instability waves might be the second mode of instability waves. As the nose-tip radius further increases to $R = 2$ mm, the corresponding entropy-layer swallowing length is approximately 284 mm, where the fifth PCB sensor is allocated. From Fig. 7(e) one can notice that the spectra amplitudes of instability waves ranging from 100 kHz to 250 kHz decrease dramatically in comparison with those with smaller nose tip radiuses, denoting that the boundary-layer transition has been efficiently delayed. The content of the spectra over 300 kHz was observed in the experiment of Kennedy et al. [23], and can be attributed to the resonance effect of the PCB sensor. For the 5 mm nose tip case, however, the bumps denoting instability waves disappear suddenly. Moreover, the broadband spectra are smaller than those of all the other nose-tips. Recalling that the predicted entropy-layer swallowing distance for $R = 5$ mm case is expected to cover the overall cone model, it is thus reasonable to speculate that conventional linear stability waves are absent when the entropy layer is dominant although the so-called nonmodal instability is either invisible. The general trend of the boundary-layer transition delay follows the work reported by Stetson and Rushton [16], and also Grossir et al. [20].

For the sake of characterizing the instability waves measurement by flush-mounted PCB sensors, the time transients of wall pressure fluctuation with different nose-tips are filtered with a bandwidth between 100 kHz and 300 kHz, as depicted in Fig. 8. The evolution of wave packages represents the growth of instability waves for small nose-tips. When the nose-tip radius increases to $R = 1$ mm, the instability waves measured by the first three sensors attenuate quickly. At $R = 5$ mm the pressure traces exhibit no characteristic content of instability waves. Based on the filtered pressure traces comparison, it is confident to believe that the boundary layer retains laminar for all nose-tips, and moreover, the large nose-tip radius case should correspond to a more stable laminar boundary layer.

Next, the convective velocity of the wave package is calculated based on the cross-correlation analysis. Shown in Fig. 9 is the cross-correlation for the first 5 PCB sensors for $R = 0.1$ mm, and four group velocities of the instability waves are obtained. The group velocity ranges from $0.84U_e$ to $0.87\ U_e$, following the property of second mode of instability waves [32]. It is thus concluded that at a low Reynolds number, the instability waves measured with interchangeable nose-tips are the second mode instability, and the entropy-layer swallowing distance shifts the linear stable region rearward as the radius of the nose-tip increases, resulting in a more suppressed growth of the second mode instabilities.

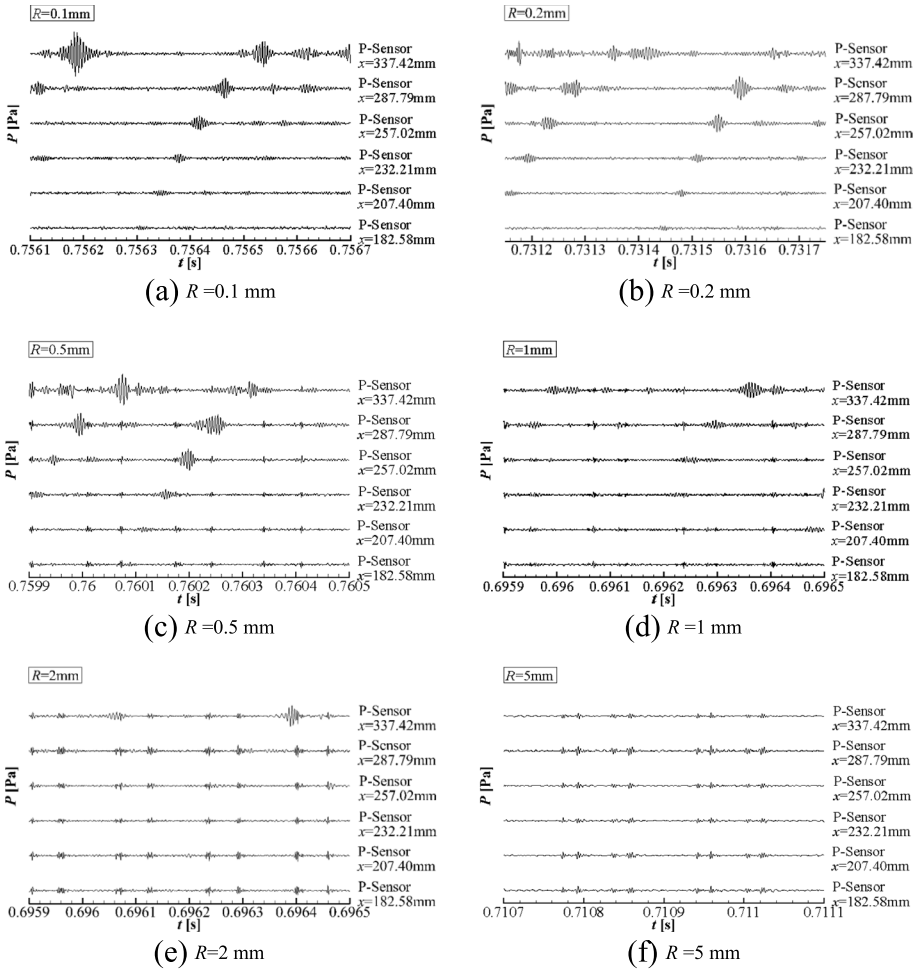

Fig. 8 Time transient of PCB sensors with Re_{unit} = 4E+6/m and filter bandwidth 100 kHz - 300 kHz

4.3 Entropy-layer effect at an intermediate Reynolds number Re_{unit} = 6E+6/m

As the freestream unit Reynolds number increases to 6E+6/m, the entropy-layer swallowing length is larger than that of the lower Reynolds number according to Fig. 5. The PSD of pressure fluctuation with different cone tips is given in Fig. 10. When the tip radius is 0.1 mm, instability waves ranging from 180 kHz to 340 kHz are found along the cone model, indicating a fully laminar boundary-layer. As the cone tip goes to $R = 1$ mm, the spectra distribution is much like that of the case of $R = 0.1$ mm except that the amplitude of the instability waves measured by the first three PCB sensors is lower, denoting the suppression of instability waves by the displacement of entropy-layers. When the tip radius goes to 2 mm, the influence is obvious that the amplitudes of the instability waves attenuate fast for the first three sensors. As the tip radius comes to 5 mm, all the instability waves vanish in the same manner as that of Re_{unit} = 4E+6/m.

In the same way, the group velocity of the instability waves is calculated based on the cross-correlation method, and the corresponding values are given in Table 2. The average group velocity of the visible instabilities waves is about $0.86U_e$, which should correspond to the second mode instability waves.

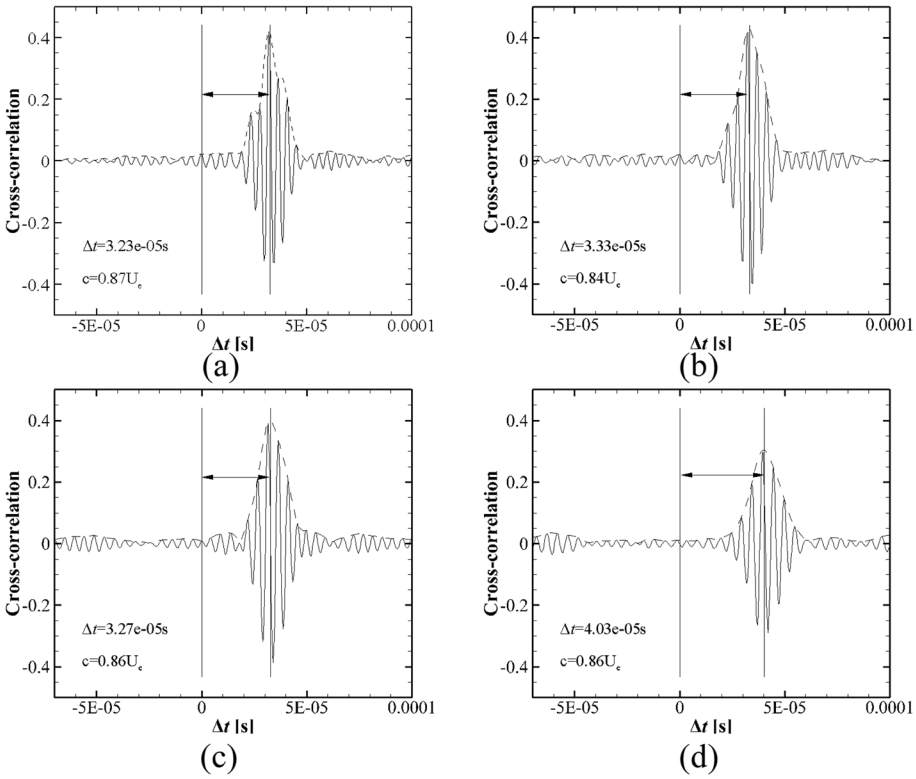

Fig. 9 Group velocity of second mode instability wave package based on bluntness of $R = 0.1$ mm, **a** Sensor NO. 1 → NO. 2, **b** Sensor NO. 2 → NO. 3, **c** Sensor NO. 3 → NO. 4, **d** Sensor NO. 4 → NO. 5, $Re_{unit} = 4E+6/m$

4.4 Entropy-layer effect at Reynolds number $Re_{unit} = 10E+6/m$

To obtain a better insight into the evolution of instability waves, the unit Reynolds number of freestream is increased to 10E+6/m. Listed in Table 3 is the entropy-layer swallowing distance for different nose-tips at $Re_{unit} = 10E+6/m$, and one can notice that the entropy-layer swallowing distance almost covers the entire cone model when the nose-tip radius reaches 2.0 mm.

The spectra of wall pressure fluctuation are given in Fig. 11. At small nose-tips, only the last two PCB sensors can detect instability waves ranging from 240 kHz to 500 kHz. When the nose-tip radius is 0.5 mm, instability waves can be found for the first five sensors, and more interestingly, instability waves are observed for all the sensors when the tip radius is 1 mm or 2 mm. This can be explained by the increased entropy-layer swallowing distance, which suppresses the growth of second mode instability waves. As the tip radius increases to $R = 5$ mm, the instability waves disappear except for a small bump for the last PCB sensor from 120 to 210 kHz. Based on this measurement, it is prominent that the entropy-layer swallowing length delays the boundary-layer transition as the nose-tip radius increases.

Additionally, the pressure traces of PCB sensors are represented in Fig. 12. When the nose-tip radius is 0.1 mm and 0.2 mm, the first two sensors exhibit instability wave packages, whereas the rest of the sensor signals show turbulent boundary-layer status. When the nose-tip radius is 0.5 mm, instability wave packages are observed for

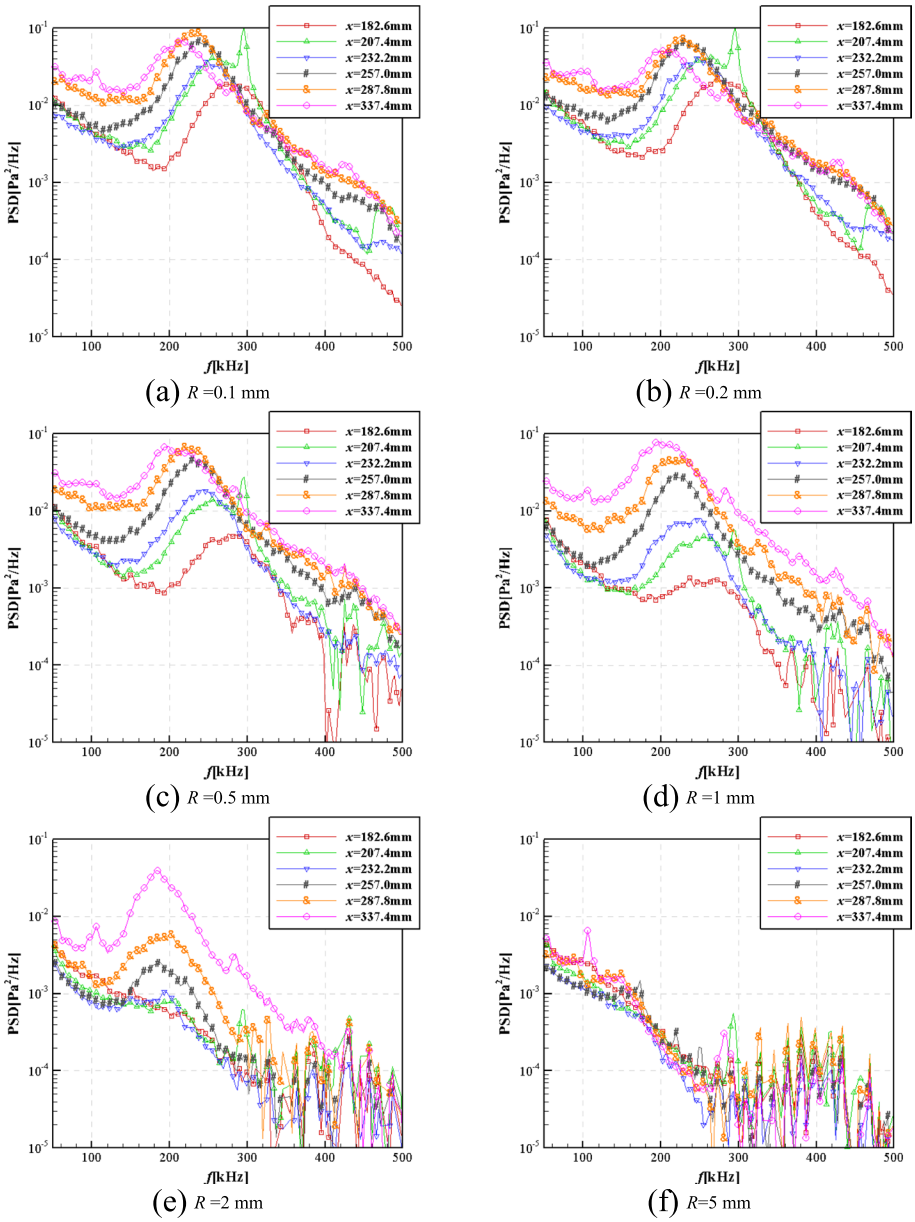

Fig. 10 PSD of wall pressure fluctuations at different cone bluntness. The wall temperature of the cone model is 300 K, the stagnation pressure of the wind tunnel is 6E+ 5 Pa, the stagnation temperature of the wind tunnel is 454 K, and the corresponding Reynolds number is 6E+ 6/m

Table 2 Cross-correlation of the first four PCB sensors, $Re_{unit} = 6E+6/m$

	NO. 1 → NO. 2	NO. 2 → NO. 3	NO. 3 → NO. 4	NO. 4 → NO. 5
Δx (mm)	25	25	25	30
Δt (μs)	32.3	33.3	32.7	40.3
U/U_e	0.87	0.84	0.86	0.86

the first five sensors. When the nose-tip radius goes to $R = 2$ mm, wave packages are only obvious for the last four sensors, although weak instability waves can still be observed in Fig. 12(e). At the largest nose-tip case, the pressure traces represent a full laminar boundary layer status.

Table 3 Entropy-layer swallowing distance along 7-degree half-angle cone model, Re_{unit} = 10E+6/m

Re_{unit} (1/m)	R (mm)	Ma	x_{sw} (mm)
10E+6	0.1	6	7.10
10E+6	0.2	6	17.89
10E+6	0.5	6	60.70
10E+6	1.0	6	152.96
10E+6	2.0	6	385.45
10E+6	5.0	6	1307.83

In the same way, the convective velocity is calculated for the instability waves shown in Fig. 11(d) using the cross-correlation method, as seen in Table 4. The normalized group velocity is generally between 0.83 and 0.89, indicating the properties of the second mode instability waves.

Additionally, the power spectral density for different tip radiuses is consolidated to reveal the influence of bluntness to instability waves with different Reynolds numbers, as shown in Fig. 13. Within this comparison, only the PSD of the first and last sensors is included. At a low Reynolds number of Re_{unit} = 4E+6/m, the second mode instability waves show up when small to moderate radiuses are applied. When the tip radius is R = 1 mm, the second mode instability disappears, and moreover, it is noticed that the amplitudes of the spectra keep decreasing when the bluntness further increases. As attention is shifted to the last PCB sensor with the same freestream Reynolds number, it is found that the modal instability waves still exist when the nose-tip radius is 2 mm, and the amplitude of instability waves is generally higher than that of the NO. 1 sensor. This demonstrates that the modal instability waves keep growing as they develop downstream with Re_{unit} = 4E+6/m, that is to say, the second mode instability is still the dominant instability when the noise-tip is less than 2 mm.

Moreover, the bi-spectra analysis is conducted. Note that the spectra of the obtained bicoherence coefficients bic^2 quantitatively reflect the degree of nonlinear interactions of the quadratic type for three waves with frequencies $f_1, f_2, f_3 = f_1 + f_2$ [33]. Figure 14 shows the bicoherence coefficients contour for the PCB sensor NO. 1 at Re_{unit} = 10E+6/m, corresponding to the images in Fig. 13(e) and (f). When the nose tip radius is smaller than 1 mm, nonlinear interactions are obvious for the second mode instabilities, implying that the energy exchange between the instability waves through phase-locked mechanism at (400 kHz, 400 kHz). Moving on to R = 2 mm, the nonlinear interactions begin to decay, denoting that the nonlinear interactions are no longer quadratic [34]. This phenomenon can also be reflected from the PSD in Fig. 13(e) that at a large nose tip radius, the amplitude of the second mode instability waves is relatively weak.

As attention is turned to the NO. 6 PCB sensor in Fig. 15, nonlinear interactions are visible for the case of tip radius of 1 mm and 2 mm, as the second mode instabilities are absent for all the other cases. Note that there is no nonlinear interaction when the tip radius is 5 mm, despite disturbance ranging from 100 to 200 kHz observed in Fig. 13(f).

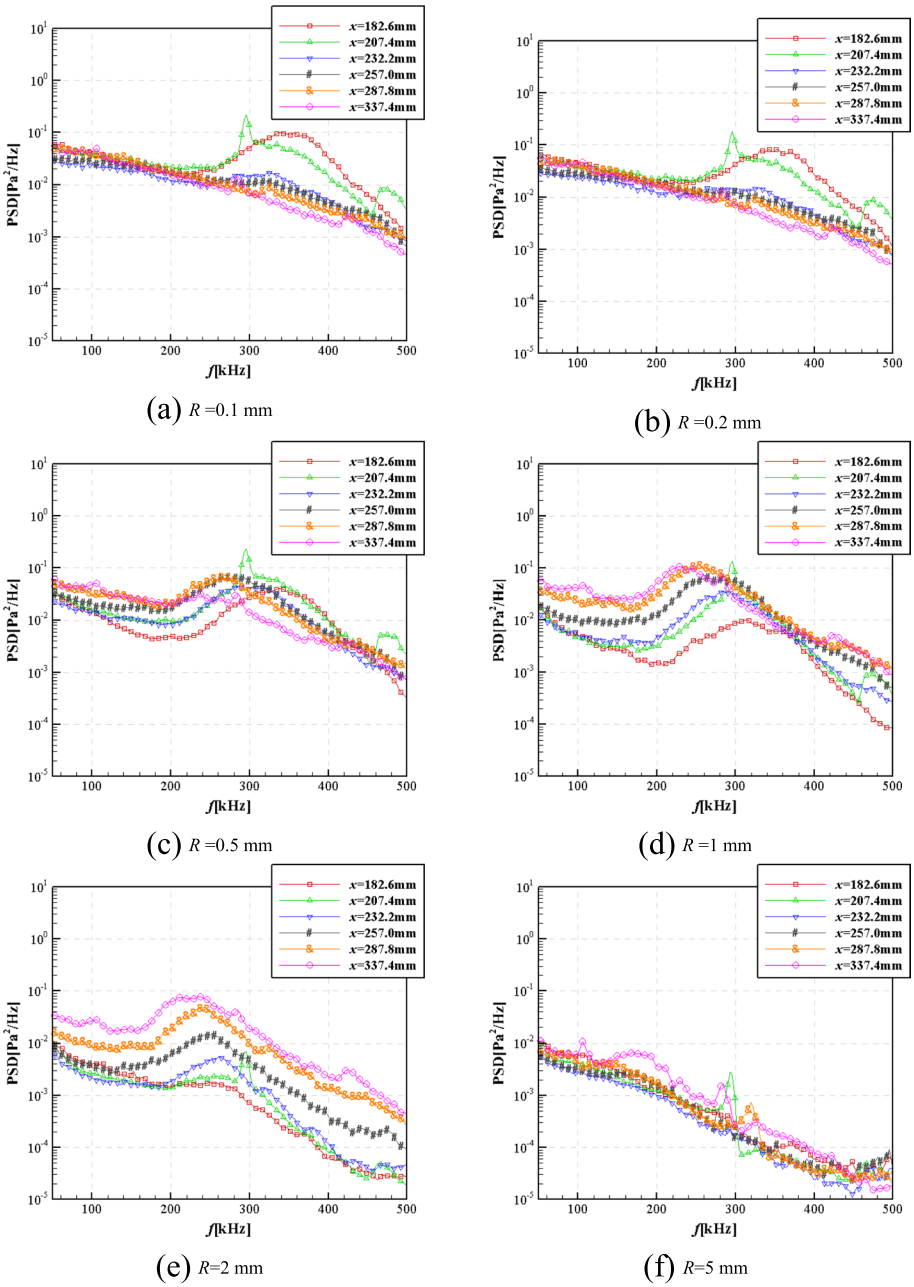

Fig. 11 PSD of wall pressure fluctuations at different cone bluntness. The wall temperature of the cone model is 300 K, the stagnation pressure of the wind tunnel is 10E+5 Pa, the stagnation temperature of the wind tunnel is 454 K, and the corresponding Reynolds number is 10E+6/m

5 Conclusion

In this work, we investigated the influence of nose tip bluntness on the hypersonic boundary-layer transition in a noisy Ludwieg tube tunnel with the aid of surface mounted pressure sensors before the so-called transition reversal phenomenon occurs. The evolution of instability waves along the streamwise direction with different nose tips was characterized by PSD as well as the cross-correlation calculation, together with the entropy-swallowing distance analysis. The PSD results reveal

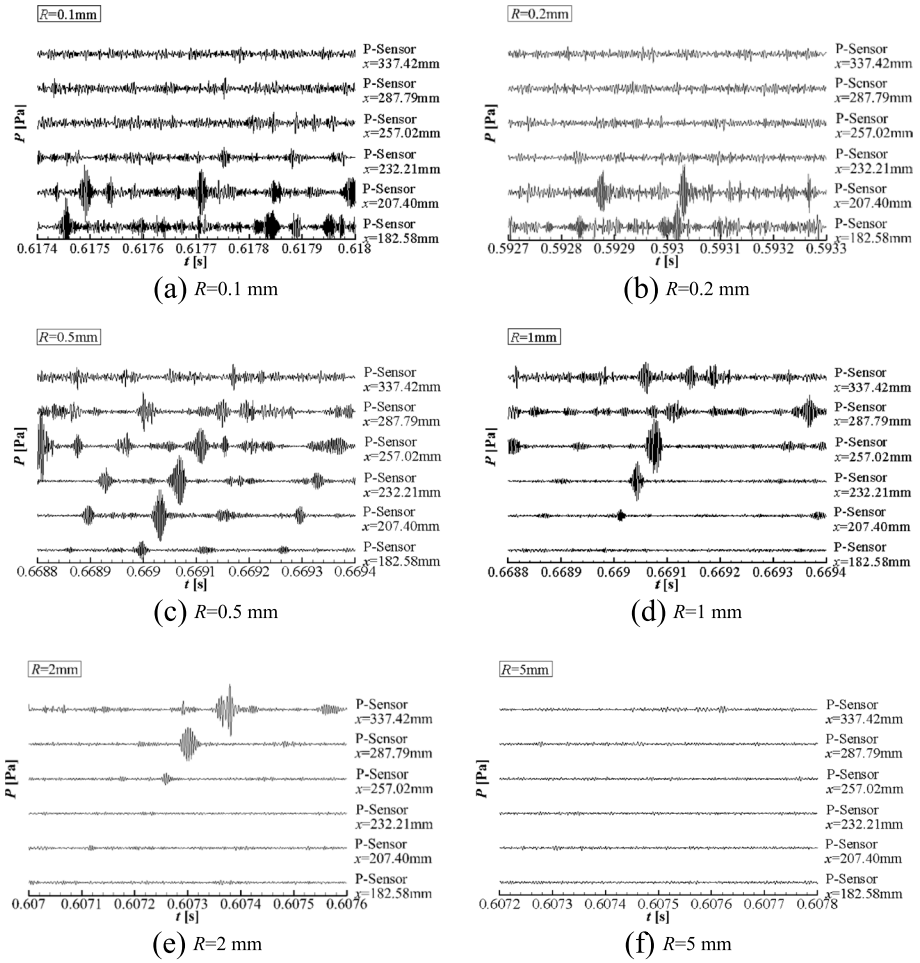

Fig. 12 Time transient of PCB sensors with Re_{unit} = 10E+6/m and filter bandwidth 150 kHz - 400 kHz

Table 4 Cross-correlation of the first four PCB sensors, Re_{unit} = 10E+6/m

	NO. 1 → NO. 2	NO. 2 → NO. 3	NO. 3 → NO. 4	NO. 4 → NO. 5
Δx (mm)	25	25	25	30
Δt (μs)	34.0	31.7	33.7	41.33
U/U_e	0.83	0.89	0.83	0.84

that the nose tip radius has little influence on the evolution of instability waves along the hypersonic boundary-layer when it is smaller than 0.2 mm; as the nose tip increases to a moderate size, the hypersonic boundary layer transition is delayed monotonically as the nose tip radius increases, and this can be explained by the downstream-shifting of entropy-swallowing distance as the nose tip radius becomes large [18]. When the nose tip radius comes to an even larger size, i.e., $R = 5$ mm, the instability waves along the hypersonic boundary-layer are strongly suppressed, and the hypersonic boundary-layer exhibits laminar status without instability waves. This trend agrees well with that obtained by Grossir et al. [20] and Kennedy et al. [23], but the so-called non-modal instabilities [23] are not observed within the current unit

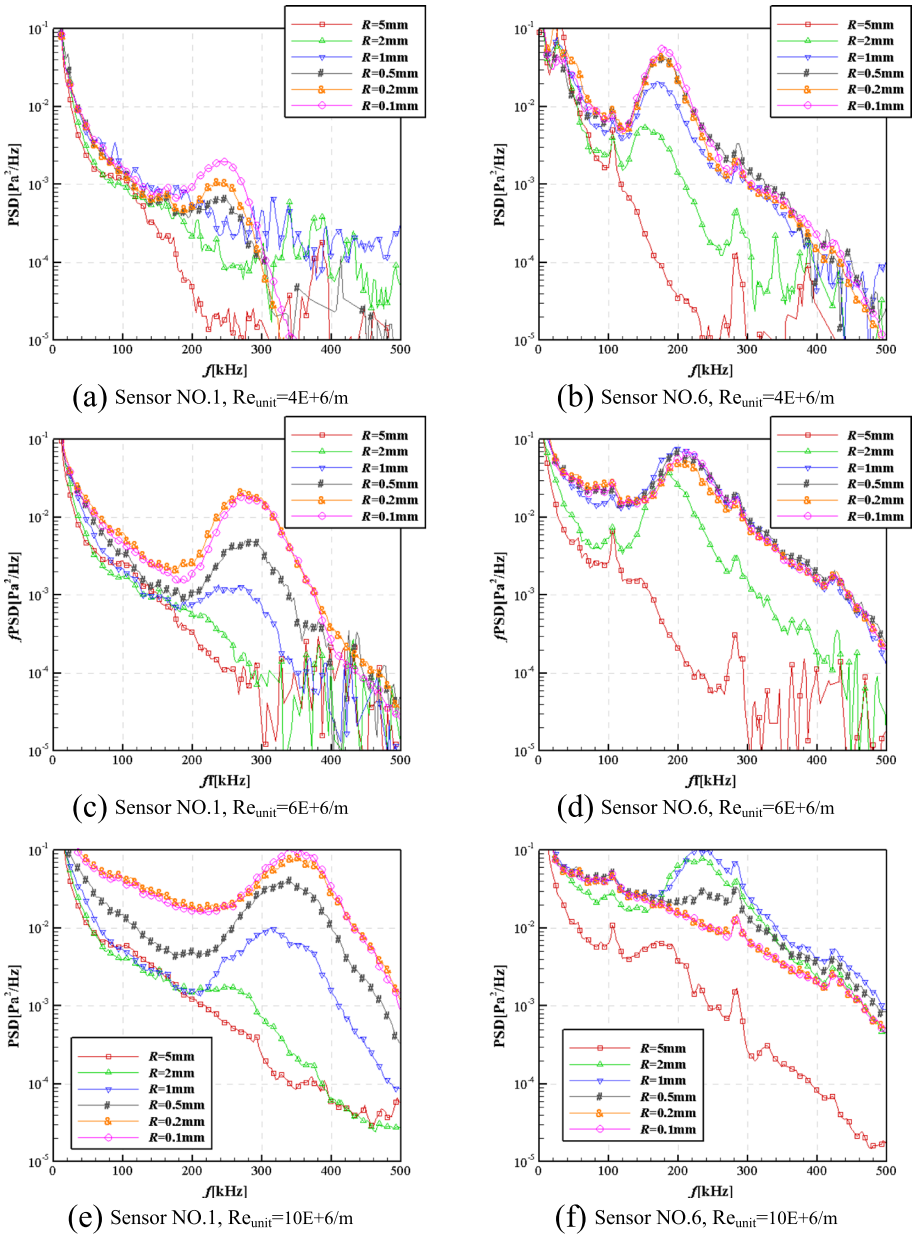

Fig. 13 PSD of wall pressure fluctuations at different streamwise locations. Sensor NO. 1 is located at $x = 182.6$ mm, while sensor NO. 6 is located at $x = 337.4$ mm

Reynolds number range. The group velocity deduced by cross-correlation calculation indicates that the instability waves observed herewith are the second mode instability waves, although disturbances ranging from 100 to 200 kHz are observed when the nose tip radius is 5 mm at a high unit Reynolds number. Bispectral analysis identifies the quadratic phase locking of second mode instabilities and it attenuates as the nose tip radius increases. In general, the second mode instability waves still play the dominant role in the hypersonic boundary layer transition as the nose tip radius increases once they exist, despite they disappear when the nose tip radius increases to a certain value. Through this experimental study, the characteristics of instability waves along

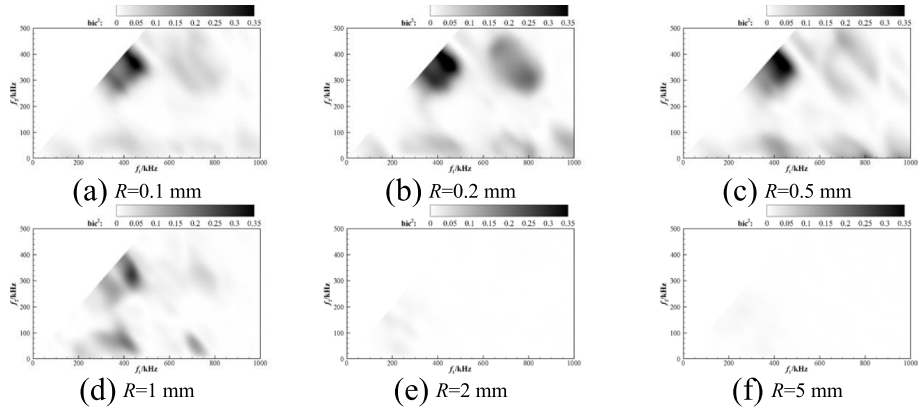

Fig. 14 Bicoherence contour of instability wave interactions measured by the PCB sensor NO.1 at $Re_{\text{unit}} = 10E+6/m$

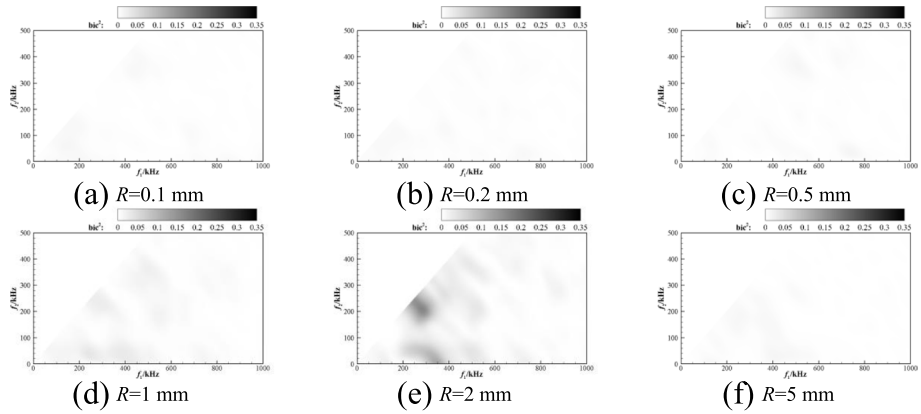

Fig. 15 Bicoherence contour of instability wave interactions measured by the PCB sensor NO. 6 at $Re_{\text{unit}} = 10E+6/m$

the hypersonic boundary-layer with interchangeable nose tips have been surveyed comprehensively. In future work, efforts will be made to resolve the eigen-function within the entropy-layer swallowing region using non-intrusive techniques, and also attention will be placed on the completive mechanism of co-existing instabilities on slender cone model when the freestream Reynolds number further increases.

Acknowledgements
Not applicable.

Authors' contributions
All authors have read and agreed to the published version of the manuscript.

Funding
This work was supported by the National Natural Science Foundation of China (Grant No. 92052301).

Availability of data and materials
The data presented in this study are available from the corresponding author upon reasonable request.

Declarations

Competing interests
The authors declare that they have no conflict of interest regarding this work.

Received: 1 August 2022 Accepted: 2 October 2022
Published online: 02 November 2022

References

1. Yu P, Duan Y, Chen J (2015) Some aerodynamic issues in hypersonic flight. Acta Aeronaut Astronaut Sin 36(1):7–23
2. Sun X, Huang W, Ou M et al (2019) A survey on numerical simulations of drag and heat reduction mechanism in supersonic/hypersonic flows. Chin J Aeronaut 32(4):771–784
3. Fedorov A (2011) Transition and stability of high-speed boundary layers. Annu Rev Fluid Mech 43:79–95
4. Reed HL, Perez E, Kuehl J et al (2013) Hypersonic stability and transition prediction. Paper presented at the 21st AIAA computational fluid dynamics conference, San Diego, 24–27 June 2013
5. Schneider SP (2004) Hypersonic laminar–turbulent transition on circular cones and scramjet forebodies. Prog Aerosp Sci 40:1–50
6. Saric WS, Reed HL, White EB (2003) Stability and transition of three-dimensional boundary layers. Annu Rev Fluid Mech 35:413–440
7. Lee C, Chen S (2019) Recent progress in the study of transition in the hypersonic boundary layer. Natl Sci Rev 6(1):155–170
8. Lee CB, Wu JZ (2008) Transition in wall-bounded flows. Appl Mech Rev 61(3):030802
9. Lee C, Jiang X (2019) Flow structures in transitional and turbulent boundary layers. Phys Fluids 31:111301
10. Chen J, Tu G, Zhang Y et al (2017) Hypersnonic boundary layer transition: what we know, where shall we go. Acta Aerodyn Sin 35(3):311–337
11. Luo J (2015) Transition and prediction for hypersonic boundary layers. Acta Aeronaut Astronaut Sin 36(1):357–372
12. Xie S, Yang W, Shen Q (2015) Review of progresses in hypersonic boundary layer transition mechanism and its applications. Acta Aeronaut Astronaut Sin 36(3):714–723
13. Schneider SP (2001) Hypersonic laminar instability on round cones near zero angle of attack. Paper presented at the 39th aerospace sciences meeting and exhibit. Reno, 8–11 January 2001
14. Stetson KF, Thompson ER, Donaldson JC et al (1984) Laminar boundary layer stability experiments on a cone at Mach 8, part 2: blunt cone. Paper presented at the 22nd aerospace sciences meeting. Reno, 9–12 January 1984
15. Stetson KF (1983) Nosetip bluntness effects on cone frustum boundary layer transition in hypersonic flow. Paper presented at the 16th fluid and plasmadynamics conference, Danvers, 12–14 July 1983
16. Rushton GH, Stetson KF (1967) Shock tunnel investigation of boundary-layer transition at $M = 5.5$. AIAA J 5(5):899–906
17. Softley EJ (1968) Transition of the hypersonic boundary layer on a cone: part II. Experiments at $M = 10$ and more on blunt cone transition. General Electric Co Tech Rep R68SD14
18. Lei J, Zhong X (2012) Linear stability analysis of nose bluntness effects on hypersonic boundary layer transition. J Spacecr Rockets 49(1):24–37
19. Jewell JS, Kimmel RL (2017) Boundary-layer stability analysis for Stetson's Mach 6 blunt-cone experiments. J Spacecr Rockets 54(1):258–265
20. Grossir G, Pinna F, Chazot O (2019) Influence of nose-tip bluntness on conical boundary-layer instabilities at Mach 10. AIAA J 57:3859–3873
21. Paredes P, Choudhari MM, Li F (2016) Nonlinear transient growth and boundary layer transition. Paper presented at the 46th AIAA fluid dynamics conference, Washington, 13-17 June 2016
22. Paredes P, Choudhari MM, Li F et al (2019) Nose-tip bluntness effects on transition at hypersonic speeds. J Spacecr Rockets 56(2):369–387
23. Kennedy RE, Jewell JS, Paredes P, Laurence SJ (2022) Characterization of instability mechanisms on sharp and blunt slender cones at Mach 6. J Fluid Mech 936:A39
24. Zhao J, Sima X, Huang R et al (2022) Design of a hypersonic Ludwieg tunnel with a double-bent storage tube. Acta Aerodyn Sin 40(4):90–100
25. Huang R, Sima X, Cheng J et al (2021) Hypersonic boundary-layer transition experiments in Ludwieg tube. Phys Gases 6(5):51–61 (in Chinese)
26. Li Z, Xiong Y, Yuan X et al (2022) A-variant design of hypersonic Ludwieg tube wind tunnel. AIAA J60(7):3990–4005
27. Chokani N (2005) Nonlinear evolution of Mack modes in a hypersonic boundary layer. Phys Fluids 17:014102
28. Bountin D, Shiplyuk A, Maslov A (2008) Evolution of nonlinear processes in a hypersonic boundary layer on a sharp cone. J Fluid Mech 611:427–442
29. Rotta N (1966) Effects of nose bluntness on the boundary layer characteristics of conical bodies at hypersonic speeds. New York University, TR NYUAA-66-66, New York
30. Heitmann D, Kähler C, Radespiel R et al (2008) Disturbance-level and transition measurements in a conical boundary layer at Mach 6. Paper presented at the 26th AIAA aerodynamic measurement technology and ground testing conference, Seattle, 23–26 June 2008
31. Munoz F, Wu J, Radespiel R et al (2019) Freestream disturbances characterization in Ludwieg tubes at Mach 6. Paper presented at the AIAA SciTech 2019 Forum, San Diego, 7–11 January 2019
32. Stetson KF, Kimmel RL (1992) On hypersonic boundary-layer stability. Paper presented at the 30th aerospace sciences meeting and exhibit, Reno, 6–9 January 1992
33. Bountin D, Maslov A (2017) Analysis of the development of perturbations in a hypersonic boundary layer behind a wavy surface. Tech Phys Lett 43:623–626
34. Craig SA, Humble RA, Hofferth JW, Saric WS (2019) Nonlinear behaviour of the Mack mode in a hypersonic boundary layer. J Fluid Mech 872:74–99

Publisher's Note